Regular Article

PHYSICAL CHEMISTRY RESEARCH
Published by the
Iranian Chemical Society
www.physchemres.org
info@physchemres.org

Phys. Chem. Res., Vol. 14, No. 1, 195-208, March 2026
DOI: 10.22036/pcr.2025.558955.2783

A Magnetic $CuFe_2O_4$@MXene/g-C_3N_4 Composite for Efficient Visible-Light Degradation of Dyes and Pharmaceuticals

Z. Sayadi, E. Ghasemian Lemraski* and Z. Tahmasebi

Faculty of Science, Department of Chemistry, Ilam University, Ilam, Iran

(Received 12 November 2025, Accepted 3 January 2026)

In this study, we developed a novel magnetic composite material by integrating $CuFe_2O_4$ nanoparticles onto MXene nanosheets *via* a co-precipitation method, and subsequently loading it onto g-C_3N_4. The aim was to enhance the photocatalytic properties for environmental remediation, particularly the degradation of organic pollutants. The structural, optical, and photocatalytic properties of the $CuFe_2O_4$@MXene/g-C_3N_4 composite were thoroughly characterized using photoluminescence, Raman spectroscopy, SEM, EDX, DRS, VSM, XRD, and FT-IR techniques. The results showed that each component, $CuFe_2O_4$, MXene, and g-C_3N_4, played a crucial role in improving the composite's photocatalytic efficiency. Specifically, $CuFe_2O_4$ enhanced visible light absorption and charge separation, MXene provided a stable 2D platform for nanoparticle dispersion, and g-C_3N_4 extended the light absorption range while introducing additional active sites. As a result, the composite exhibited superior degradation efficiency for methylene blue, methyl orange, and ibuprofen compared to the individual components. This work demonstrates the potential of this composite material for effective environmental applications, offering a promising approach for the degradation of organic pollutants under visible light.

KEYWORDS: MXene, Photocatalyst, Azo dyes, Graphitic carbon nitride, Synergism

INTRODUCTION

The water crisis is a significant global challenge that has been a growing concern for many years and is expected to continue impacting various regions around the world in the 2020-2030 timeframe. Efforts to mitigate the water crisis in the 2020-2030 timeframe will require a combination of strategies and actions. While addressing the water crisis is a complex and ongoing challenge, concerted efforts at the local, national, and global levels can help mitigate its impacts and ensure sustainable access to clean water for all [1-4]. Water recycling and desalination are two important strategies for addressing water scarcity and ensuring a sustainable supply of freshwater, especially in regions facing water stress [5,6]. These processes have distinct approaches and applications, each with its advantages and considerations. Water recycling, also known as water reuse or wastewater reclamation, involves treating and reusing wastewater from various sources for various purposes. This can include filtration, coagulation and flocculation, adsorption, and photocatalytic degradation methods [7]. Photocatalysts, typically made of semiconductor materials like titanium dioxide (TiO_2) and other advanced materials, can play a significant role in water treatment processes by harnessing the power of light to facilitate chemical reactions [8]. The primary application of photocatalysts in water treatment is for the degradation of organic pollutants, the disinfection of water, and the removal of harmful microorganisms. Photocatalysts can break down organic contaminants, including dyes, pesticides, pharmaceuticals, and industrial chemicals, into harmless substances. Several materials have been studied and developed as photocatalysts such as titanium dioxide (TiO_2), zinc oxide (ZnO), bismuth vanadate ($BiVO_4$), tungsten trioxide (WO_3), graphitic carbon Nitride (g-C_3N_4), semiconductor metal sulfides (*e.g.*, CdS, ZnS), perovskite materials (*e.g.*, $LaFeO_3$, $SrTiO_3$), hydrogenated

*Corresponding author. E-mail: e.ghasemian@ilam.ac.ir

titanium dioxide (H-TiO_2), and, metal-organic frameworks (MOFs). g-C_3N_4 is a metal-free photocatalyst that is stable, environmentally friendly, and responsive to visible light. It is used for the degradation of organic pollutants, hydrogen generation, and other applications [10-12]. Researchers are continually developing and improving photocatalyst materials to enhance their performance, stability, and versatility in various environmental and industrial applications. In the present research, we try to modify g-C_3N_4 with $CuFe_2O_4$ doped on MXene nanosheet. The band gap of the composite material can be tuned by controlling the doping concentration of $CuFe_2O_4$ in MXene and the loading amount of the composite on g-C_3N_4. This can influence the photocatalytic performance by affecting the absorption of light and the generation of electron-hole pairs. The structural, electrical, optical, and photocatalytic activities have been determined to investigate the main properties in detail. Understanding the mechanisms of light-induced charge transfer between different components of the composite (*e.g.*, g-C_3N_4, $CuFe_2O_4$, and MXene) is vital. This knowledge can help optimize the material for specific applications, such as enhancing photocatalytic activity.

EXPERIMENTAL

Materials and Methods

The precursor Ti_3AlC_2 powder (purity > 98 wt%) was purchased from Tabibshimi Co., Ltd. HF, $CuCl_2.2H_2O$, $FeCl_3.6H_2O$, NaOH, methyl orange, metylene blue, and ethanol were purchased from Merck company. Ibuprofen was purchased from Behsa Company (Arak, Iran).

Composite Preparation

A 7% hydrofluoric acid (HF) solution in water was prepared. This solution is used as an etchant to selectively remove aluminum from the MAX phase, yielding MXene. A specific amount of MAX phase was mixed with 10 ml of HF7% and stirred for 24 h. Stirring facilitates the etching process and helps in obtaining a homogeneous MXene product. The appearance of bubbles during the stirring process indicates the proper progression of the etching reaction. This observation suggests that the aluminum layer is being effectively removed from the MAX phase. After the 24-hour stirring of the MXene with double-distilled water, washed to remove residual HF and by-products. Washing continued until the pH of the solution approached neutrality. This ensures that any remaining acidic components are thoroughly removed from the MXene. Finally, the remaining residue in the solution is dried in a vacuum at 70 °C for 24 h [13-16]. The characteristic analysis of MXene is given in the supporting materials.

$CuFe_2O_4$ Loading on MXene Nanosheet

Initially, 0.0108 g of the MXene sample was accurately weighed and dispersed in 50 ml of deionized water and sonicated for 15 min using an ultrasonic device. In the next step, 0.111 g of copper chloride ($CuCl_2$) and 0.352 g of iron chloride ($FeCl_3$) were added to the previous solution. The mixture was allowed to react on a stirrer for 30 min. Subsequently, NaOH (0.1 M) solution was added dropwise to adjust the pH = 10. Following this step, the solution was placed on a heater-stirrer at a temperature of 50 °C, and the stirring continued for 3 h to promote further reaction. After this 3-hour period, the solution was transferred to an autoclave at 120 °C for 12 h. In the final step, the obtained precipitate was placed in a vacuum oven and dried for 12 h at 60 °C. At this stage, fine and dark-brown color precipitates were obtained. To obtain g-C_3N_4, first, melamine, which is a soft, lightweight, and white powder, should be placed in a furnace at a temperature of 550 °C for 4 h. The resulting powder is firm and yellow after exiting the furnace. By adding 0.02 g of g-C_3N_4 to 50 ml of deionized water, and sonicated for one hour. Then, the g-C_3N_4 mixture and $CuFe_2O_4$@Mxene Solution were mixed and stirred for 6 h at 70 °C to gradually evaporate the solvent. The remained composite was dried at 60 °C in a vacuum oven for 12 h [18-20].

Photo-catalytic Efficiency Test

In order to investigate the catalytic efficiency, the efficacy of three compounds in the degradation of two anionic and cationic dyes, as well as the drug ibuprofen, was experimentally examined at various concentrations (5,15, and 20 ppm) and durations, and the results were analyzed. The solutions were initially allowed to reach equilibrium for 30 min in a dark environment. Subsequently, every twenty minutes at 25 °C, samples were withdrawn from the solutions, centrifuged, and the amount of dye and drug was

determined using a UV-Vis spectrophotometric [21]. We used a Visible-light LED source with a wavelength range between 420-700 nm, main emission peak: 450 nm, power: 150 W, and distance from the sample: 8 cm.

Characterization

The microscopy image of the prepared nanocomposite is given by Field Emission Scanning Electron Microscopy (FESEM, QUANTA FEG-450**,** FEI, USA). The crystalline structure nanocomposite was indicated using an X Ray Diffractometer (PW1730, PHILIPS Company, Netherlands). Fourier transform infrared (FTIR) spectroscopy was performed by Bruker-Germany VBRTEX70 spectrometer. Absorption of solution was measured by UV-Visible spectrophotometer model Cary 300, Agilent, Germany. The surface area was identified based on the Micrometrics Surface Area Analyzer (Belsorp-miniII, BEL Japan). The magnetic properties of the samples were investigated using a vibrating sample magnetometer (VSM MDKB model, Danesh Pajuh Magnetic Co., Kashan, Iran). UV-Vis diffuse reflection spectra (DRS) were performed on a UV-Vis spectrophotometer (Diffuse reflectance spectroscopy S-4100, SCINCO, South Korea) with $BaSO_4$ as the reference compound. The photoluminescence (PL) emission spectra was measured with a PL spectrophotometer (G9800A, Agilent, Germany). Raman spectroscopy was conducted using a micro-Raman spectrometer (Raman Takram P50C0R10, Iran).

RESULTS AND DISCUSSION

The chemical activity of the transition metal sites on the MXene surface can be modulated through surface functionalization of $CuFe_2O_4$, where specific chemical groups or molecules are attached to the surface. This functionalization process allows for the tailoring of surface properties to achieve desired functionalities or enhance specific interactions. To study these effects, FTIR spectra have been obtained from the samples. Figure 1 represents the FTIR spectra of all three prepared samples. The spectrum of pure MXene shows the main peaks with high intensity in the range of 600-800 cm^{-1}, corresponding to Ti-C stretching vibrations, confirming the presence of MXene layers. MXenes synthesized using aqueous HF etching typically acquire electronegative surface functional groups like –OH, –F, –O, making them hydrophilic [22,23]. Oxygen-containing functional groups in the MXene, and the bending vibration of the OH bond, show peaks in the region of 1200-1800 cm^{-1}. The broad peak in the range of 3000-3600 cm^{-1} is associated with O-H stretching vibrations, indicating the presence of hydroxyl groups or adsorbed water [24]. Hydroxyl groups (-OH) are one of the most common surface terminations of MXene materials. These terminations occur due to the presence of oxygen-containing functional groups on the surface, which can originate from the synthesis process or from exposure to air and moisture.

One noteworthy observation in the FTIR spectrum is the emergence of new peaks, indicating the successful incorporation of $CuFe_2O_4$ onto the MXene substrate. These additional peaks signify the formation of new bonds or alterations in existing functional groups, underscoring the effective loading and integration of $CuFe_2O_4$ within the MXene framework. Furthermore, shifts in the characteristic peaks of $CuFe_2O_4$@MXene composite suggest potential chemical transformations within the composite. Such shifts may be indicative of changes in oxidation states, bond strengths, or modifications in the chemical environment of specific functional groups. This information is crucial for understanding the nature of the chemical interactions and the synergistic effects between $CuFe_2O_4$ and MXene at a molecular level [25,26].

For $CuFe_2O_4$@MXene/g-C_3N_4 composite shows broad peaks related to C-N stretching vibrations. The peak at around 1250 cm^{-1} is often attributed to the stretching vibrations of the triazine units. This peak is associated with the bending vibration of N-H bonds, indicating the presence of amino groups. The peak around 808 cm^{-1} corresponds to the out-of-plane bending vibrations of tri-s-triazine units in g-C_3N_4. Peaks around 3000-3400 cm^{-1} are indicative of stretching vibrations of N-H and C-H bonds, suggesting the presence of amino and methyl groups. One prominent observation in the FTIR spectrum is the presence of new peaks, suggesting successful interactions between $CuFe_2O_4$@MXene and g-C_3N_4. The appearance of these peaks can be attributed to the formation of specific bonds or the modification of existing functional groups, indicating a strong interfacial connection between the components.

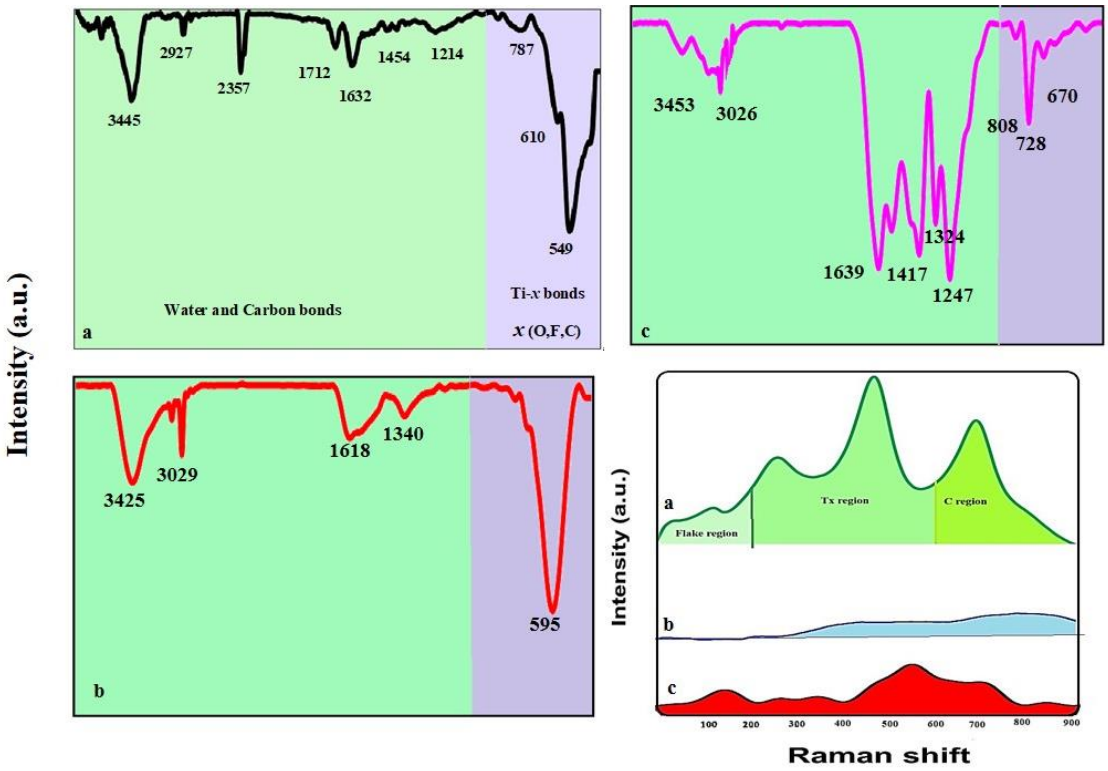

Fig. 1. FTIR and Raman spectrum of (a) MXene; (b) $CuFe_2O_4$@Mxene; (c) $CuFe_2O_4$@Mxene/g-C_3N_4.

This corroborates the effective loading and integration of $CuFe_2O_4$@MXene onto the g-C_3N_4 substrate. Furthermore, shifts in the characteristic peaks of individual components offer evidence of potential chemical transformations within the composite. These shifts can be indicative of charge transfer, hybridization, or alterations in the chemical environment of specific functional groups. The identification and interpretation of such changes contribute to a comprehensive understanding of the synergy between $CuFe_2O_4$@MXene and g-C_3N_4 at a molecular level [27]. The Raman spectrum of MXenes typically includes several characteristic peaks that arise from the vibrations of the MXene layers. Figure 2 shows that the Raman peaks at 147, 260, 428, and 615 cm^{-1} can be due to the A_{1g} and E_g active vibrations of Ti_3C_2Tx, respectively. The peak at 260 cm^{-1} corresponds to the $E_g(5)$ mode. The E_g mode involves out-of-plane vibrations of the metal atoms relative to the carbon atoms. In Ti_3C_2Tx MXene, this mode likely involves motion perpendicular to the MXene layers. Another peak at ~400 cm^{-1} corresponds to the $E_g(7)$ mode. Similar to the $E_g(5)$ mode, the $E_g(7)$ mode likely involves out-of-plane vibrations of the metal atoms relative to the carbon atoms, but with a different pattern or directionality. The band at 610 cm^{-1} also corresponds to the $E_g(4)$ mode. Again, the Eg mode signifies out-of-plane vibrations, and the $E_g(4)$ designation may indicate a particular pattern or directionality of these vibrations within the Ti_3C_2Tx MXene lattice. The specific changes observed in the Raman spectrum of MXene upon $CuFe_2O_4$ loading will depend on factors such as the loading concentration, the method of loading, and the interactions between $CuFe_2O_4$ nanoparticles and the MXene surface. When $CuFe_2O_4$ nanoparticles are loaded onto the surface of MXene, they can partially cover or block certain regions of the MXene surface. Since Raman spectroscopy relies on the scattering of photons by molecular vibrations, the presence of $CuFe_2O_4$ nanoparticles can obstruct the access of incident light to the underlying MXene layers, leading to a reduction in Raman signal intensity [28]. This behavior is confirmed in Fig. 2. The interaction between $CuFe_2O_4$ nanoparticles and MXene can induce charge transfer phenomena. This interaction can modify the electronic structure of MXene, altering its vibrational modes and affecting the intensity of

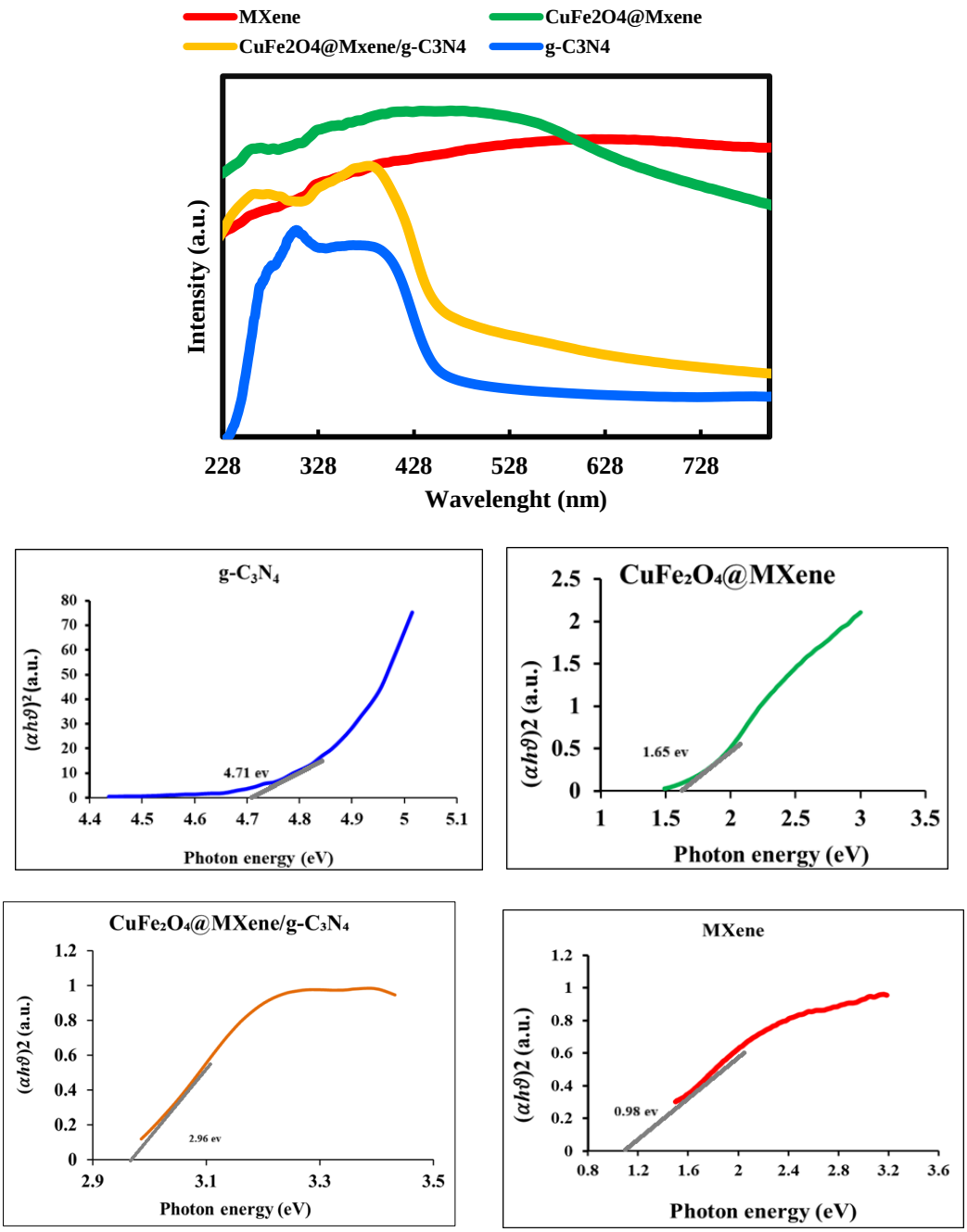

Fig. 2. UV-Vis DRS spectra, and Plot of $(\alpha h\vartheta)^2$ *vs.* photon energy of the studied samples.

Raman peaks. Charge transfer processes may redistribute charge carriers within the MXene lattice, leading to changes in the electronic density of states and consequently influencing the Raman scattering intensity [29]. Also, the deposition of $CuFe_2O_4$ nanoparticles onto MXene may induce lattice distortions or introduce defects in the MXene structure. These lattice disturbances can scatter phonons within the MXene lattice, leading to phonon relaxation processes that decrease the intensity of Raman peaks. Additionally, the presence of defects can create additional scattering centers for incident photons, further reducing the observed Raman signal intensity [30]. On the other hand, $CuFe_2O_4$ nanoparticles may possess optical properties that allow them to absorb or scatter incident light effectively. If

the excitation wavelength used for Raman spectroscopy coincides with the absorption or scattering band of $CuFe_2O_4$ nanoparticles, energy transfer mechanisms can occur. This results in the attenuation of incident light before it interacts with the MXene material, leading to a decrease in Raman signal intensity [31]. $CuFe_2O_4$ nanoparticles may exhibit surface plasmon resonance (SPR) phenomena under specific conditions, where collective oscillations of conduction electrons are excited by incident light. If the SPR band overlaps with the spectral region of MXene Raman peaks, energy transfer processes can occur between the SPR-active $CuFe_2O_4$ nanoparticles and the MXene material. This can lead to a decrease in Raman signal intensity as a result of energy absorption or scattering by the $CuFe_2O_4$ nanoparticles [32]. The addition of $CuFe_2O_4$@Mxene onto g-C_3N_4 can lead to an increase in the Raman spectrum compared to $CuFe_2O_4$@MXene. Figure 2 shows the location of repeated peaks. The very low ratio of $CuFe_2O_4$@MXene could not affect the intensity of the g-C_3N_4 Raman peak," indicating the negligible effect of $CuFe_2O_4$@MXene on the intensity of the g-C_3N_4 Raman peak. This might suggest that $CuFe_2O_4$@MXene has minimal influence on the distribution of molecular vibrations in g-C_3N_4, hence minimizing the intensity of the Raman peak. Therefore, it appears that $CuFe_2O_4$@MXene is very close to pure g-C_3N_4, and these minimal effects from $CuFe_2O_4$@MXene could be due to structural similarities with pure g-C_3N_4. MXenes exhibit interesting optical properties, including strong light absorption in the visible and near-infrared regions. DRS allows us to study the absorption spectrum of MXene powders, providing insights into their light-harvesting capabilities and potential for photocatalytic and photovoltaic applications. As can be seen in Fig. 3, pure MXene nano sheet shows the high intensity absorption spectrum in the range of visible and UV light compared to the other prepared compounds [33]. As seen from Fig. 3, the light absorption capacity of $CuFe_2O_4$@Mxene in the range of 228-428 nm shows an increasing behavior. $CuFe_2O_4$ nanoparticles possess unique optical properties, including strong light absorption in the visible and near-infrared regions. When loaded onto MXene surfaces, these nanoparticles can act as additional light absorbers, enhancing the overall light absorption capacity of the composite material. This increased light absorption leads to higher DRS intensity due to more efficient light harvesting. $CuFe_2O_4$ nanoparticles may exhibit surface plasmon resonance (SPR) effects, especially in the visible range, which can enhance light absorption and scattering. When combined with MXene, which has a high surface area and conductivity, the SPR effect of $CuFe_2O_4$ nanoparticles can be further amplified, leading to increased DRS intensity. The interaction between MXene and $CuFe_2O_4$ nanoparticles can facilitate charge transfer processes, such as electron transfer or excite generation.

These processes can modify the electronic structure of the composite material, affecting its optical properties and leading to changes in DRS intensity [34]. The mentioned mechanism is repeated in increasing absorption of g-C_3N_4 during loading of $CuFe_2O_4$@MXene. Changes in its DRS spectrum due to enhanced light absorption, SPR effects, charge transfer processes, and modifications in composite morphology. These changes can be crucial for optimizing the optical properties of g-C_3N_4-based composite materials for applications as photocatalysis and photovoltaics. The DRS spectrum of the prepared samples confirmed a clear absorption peak between 200-800 nm after loading of $CuFe_2O$ and $CuFe_2O_4$@MXene. The intrinsic properties of MXenes and $CuFe_2O_4$ tend to reduce the absorption edge band [35]. The band gap (E_g) values of Mxene, $CuFe_2O_4$@MXene, and g-C_3N_4 were calculated according to the Tauk equation and are as follows 0.98 eV and 1.65 eV, and 4.71 respectively, while the hybrid $CuFe_2O_4$@MXene/g-C_3N_4 band gap is approximately 2.96 eV, The MXene and $CuFe_2O_4$@MXene materials have significantly lower band gaps compared to g-C_3N_4 and the hybrid $CuFe_2O_4$@MXene .The $CuFe_2O_4$@MXene/g-C_3N_4 hybrid has a reduced band gap of 4.71 eV compared to pure g-C_3N_4, which suggests that incorporating impurities or other materials can modify its electronic properties. The $CuFe_2O_4$@MXene hybrid has a band gap of 1.65 eV, which is slightly higher than pure g-C_3N_4, indicating that this hybrid structure retains a high band gap close to that of pure g-C_3N_4. The introduction of MXene into the $CuFe_2O_4$ matrix increases the band gap from 0.98 eV to 1.65 eV. The band gap of g-C_3N_4 decreases when forming the $CuFe_2O_4$@MXene/g-C_3N_4 composite, which suggests that the composite structure can impact the electronic properties of the original materials, possibly due to interactions between the components or changes in the local electronic environment. Overall, these variations in band

gaps highlight the impact of material composition and hybridization on the electronic properties, which can be crucial for designing materials with specific electronic or optical characteristics [36].

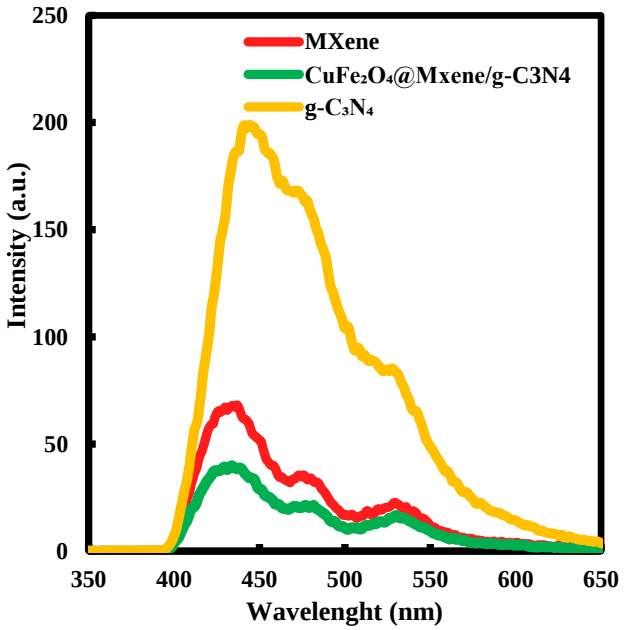

Fig. 3. Photoluminescence of the prepared samples.

When materials are photoexcited, meaning they absorb photons and become excited to higher energy states, the excess energy can be released as light when the excited electrons return to their ground state. This emission of light is known as photoluminescence. Photoluminescence emission of MXene, $CuFe_2O_4$@MXene, and $CuFe_2O_4$@MXene/g-C_3N_4 composite hybrid structures have been investigated for their potential in photoluminescence applications. As can be seen in Fig. 4, MXenes typically exhibit low or no intrinsic photoluminescence due to their metallic nature and the lack of a significant bandgap. So the electronic properties of MXenes often lead to non-radiative recombination of charge carriers, which results in minimal or no PL emission. Copper iron oxide ($CuFe_2O_4$) is a semiconductor material with interesting optical and magnetic properties. By combining MXene with $CuFe_2O_4$, it aim to introduce new functionalities and enhance the luminescent properties of the resulting composite material. Its expected $CuFe_2O_4$@MXene showed the highest separation efficiency of carriers, and high photocatalytic efficiency, respectively. Furthermore, the integration of additional materials like graphitic carbon nitride (g-C_3N_4) into $CuFe_2O_4$@MXene composites offers further opportunities for tailoring their photoluminescent properties compared to pure g-C_3N_4 [37]. XRD patterns in Fig. 4 confirmed the expected structure in the prepared composition. MXenes often show distinct peaks corresponding to the (002) and (004) planes, but the (006) and (110) peaks can also be observed depending on the specific MXene phase and its interlayer spacing. A prominent peak at 2Θ = 30º corresponds to the interlayer spacing between adjacent MXene layers. This peak is often associated with the MXene's characteristic layered structure. For MXenes, the (006) reflection is indicative of the periodicity along the c-axis of the MXene layers. The peak at 24º is related to the MXene's layered structure and corresponds to the spacing between layers and the (004) plane. It typically appears at lower 2θ angles compared to the (006) peak. The peak is part of the in-plane (103) reflections of MXenes, and it reflects the ordering in the basal plane of the MXene layers. It's an important peak for identifying the specific MXene phase.

The peak at 63º is associated with the MXene's crystal structure and can provide information on the in-plane symmetry and the arrangement of atoms within the layers. (110). Depending on the synthesis method, impurities or secondary phases may also appear in the XRD pattern. In the composite material $CuFe_2O_4$@MXene/g-C_3N_4, the XRD pattern will contain peaks from all constituent phases, along with potential shifts or broadening due to interactions between phases. Peaks corresponding to the crystallographic planes of copper iron oxide ($CuFe_2O_4$) will be present 1t. Common peaks for $CuFe_2O_4$ include (311), (400), *etc*. [38].

Figure 4 shows SEM/EDS of all three samples. MXene materials are composed of stacked layers, and SEM images reveal these layers clearly. The layers might appear as thin sheets. Loading of $CuFe_2O_4$@Mxene on g-C_3N_4 is confirmed clearly in Fig. 4b. The high titanium content with notable oxygen and lower carbon and aluminum suggests a typical MXene structure, while the composite material shows a significant increase in carbon, indicative of the presence of g-C_3N_4, along with notable amounts of iron and still a significant amount of titanium. Figure 5 shows a pronounced hysteresis loop with clear saturation magnetization and coercivity due to the ferrimagnetic nature of the prepared composite. The MXene and g-C_3N_4 are non-magnetic; they

might reduce the overall Ms of the composite. The magnetic properties of the prepared composite facilitate the recovery of catalysts from reaction mixtures. This is useful in heterogeneous catalysis processes where magnetic separation can simplify catalyst recovery and reuse. Also, the magnetic characteristics make it suitable for various applications in the fields of magnetic separation, sensors, and data storage [39].

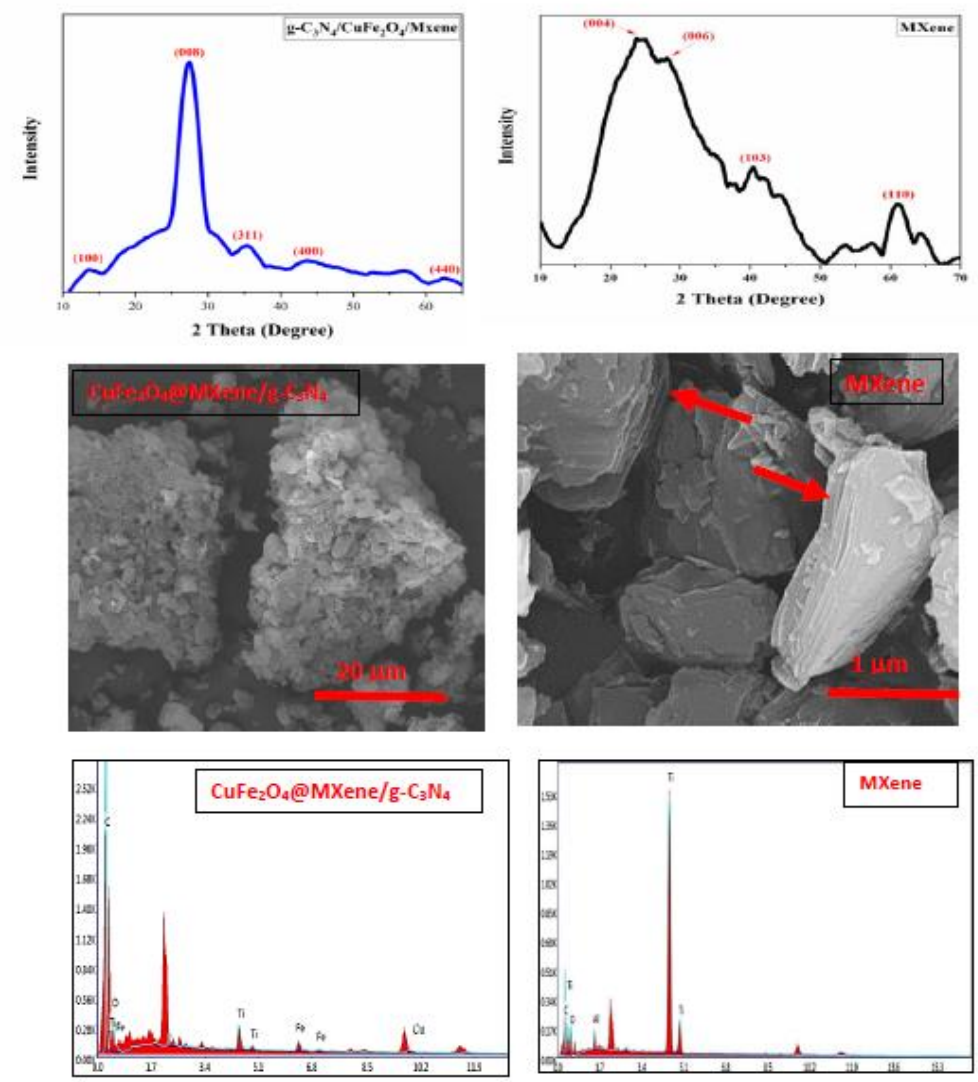

Fig. 4. XRD patterns, and SEM/EDS of MXene, and $CuFe_2O_4$@Mxene/g-C_3N_4.

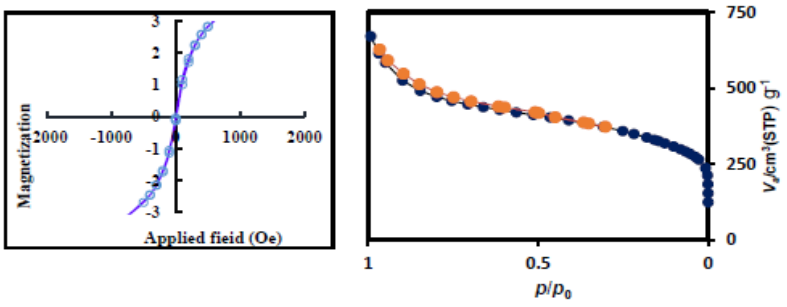

Fig. 5. VSM and N_2 adsorption/desorption isotherm of the prepared $CuFe_2O_4$@Mxene/g-C_3N_4

Table 1. Obtained Parameters Using N2 Adsorption/ Desorption (Bet) Analysis

BJH plot	
V_p	0.6544 ($cm^3\ g^{-1}$)
$r_{p,peak}(Area)$	1.22 (nm)
a_p	414.49 ($m^2\ g^{-1}$)
BET plot	
V_m	283.88 ($cm^3\ g^{-1}$)
a_s	1235.6 ($m^2\ g^{-1}$)
Total pore volume ($p/p_0 = 0.990$)	0.872 ($cm^3\ g^{-1}$)
Mean pore diameter	3.9936 (nm)

The N_2 adsorption/desorption isotherm of the prepared $CuFe_2O_4$@Mxene/g-C_3N_4 in Fig. 5 resembles a Type IV isotherm with an H_3/H_4-type hysteresis loop, which is typical for mesoporous materials (2-50 nm pores) and materials with slit-shaped pores, layered structures, or aggregates of plate-like particles (consistent with MXene and g-C_3N_4). The BET surface area of $CuFe_2O_4$@Mxene/g-C_3N_4 is 1235.6 $m^2\ g^{-1}$, which is a key factor for its performance as a photocatalyst. A high surface area provides a larger number of active sites for the adsorption of reactants such as water or pollutants, enabling a more efficient photocatalytic process. The increased surface area also enhances the material's ability to absorb light, an important feature for photocatalysis, as the efficiency of reactions like water splitting or pollutant degradation is dependent on the material's ability to absorb light and generate charge carriers (electron-hole pairs). A larger surface area provides more active sites for the adsorption of molecules like water or pollutants, essential for photocatalytic reactions such as organic pollutant degradation. The increased surface area also helps in capturing more light, crucial for driving the photochemical reactions in photocatalysis and can facilitate better separation of electron-hole pairs, reducing recombination losses and improving photocatalytic efficiency. The BJH pore size distribution reveals that $CuFe_2O_4$@Mxene/g-C_3N_4 has a mean pore diameter of 3.9936 nm**,** which places it in the mesopore range (pores between 2 and 50 nm). This is ideal for photocatalytic reactions because mesopores facilitate efficient diffusion of molecules such as pollutants into the material, allowing for easier access to the active sites on the surface. Additionally, the total pore volume (Vp = 0.6544 $cm^3\ g^{-1}$) plays an important role in the adsorption and storage of reactants. The material's ability to store significant amounts of reactants ensures that the photocatalytic reactions can occur more efficiently, as it allows for a steady supply of reactants for the process. The pore size is suitable for reactant molecules like water to enter the pores and interact with the photocatalyst's active sites. After photocatalytic reactions, products need to be desorbed from the catalyst surface. The mesopores support the release of products while preventing excessive resistance to the flow of molecules [38,39].

PHOTOCATALYTIC ACTIVITY RESULTS

In the present study, an attempt has been made to investigate and study the photocatalytic effect of the synthesized samples on the degradation of two cationic and anionic dyes, as well as a drug. Methyl orange, methylene blue, and ibuprofen were chosen respectively. The photo-degradation of methyl orange using different materials, including MXene, $CuFe_2O_4$@MXene, and $CuFe_2O_4$@MXene/g-C_3N_4, involves the use of these materials as photocatalysts to accelerate the degradation process under Vis light irradiation. Variation of concentration versus time for all studied systems are given in Fig. 6.

The results in Fig. 6a show that all of the prepared materials are good photocatalysts for methylene blue, methyl orange, and ibuprofen. MXene, being a two-dimensional material with excellent electronic conductivity and large surface area, can serve as an effective photocatalyst for the degradation of organic pollutants like methyl orange and methylene blue. MXene sheets possess abundant surface functional groups, such as hydroxyl (-OH) and oxygen-containing functional groups, which facilitate the adsorption of ionic and polar molecules onto the MXene surface. Upon exposure to light, MXene can generate electron-hole pairs due to its photoactive nature. These photo-generated electron-hole pairs can react with adsorbed oxygen molecules or water molecules to produce reactive oxygen species (ROS) such as hydroxyl radicals (•OH) and superoxide radicals. The generated ROS species attack the organic dye molecules adsorbed on the MXene surface, leading to the cleavage of

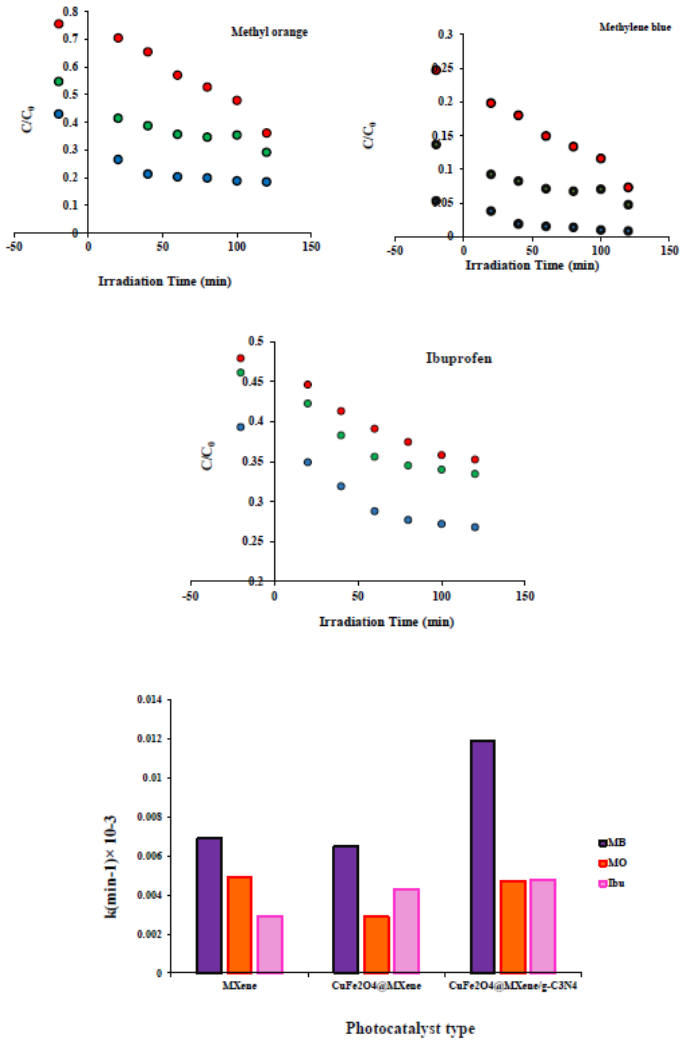

Fig. 6. Variation of methyl orange, methylene blue, and ibuprofen concentration versus time and Kinetic constants for first-order reactions in the presence of MXene, $CuFe_2O_4$@Mxene, and $CuFe_2O_4$@Mxene/g-C_3N_4.

chemical bonds and degradation of the dye molecules into smaller, less harmful products such as carbon dioxide and water. The incorporation of $CuFe_2O_4$ nanoparticles into MXene sheets can enhance the photocatalytic performance of MXene due to the synergistic effects between the two materials. $CuFe_2O_4$ nanoparticles act as light absorbers, extending the light absorption range of the composite material into the visible and near-infrared regions, where MXene alone may have limited absorption. Photo-generated electrons and holes are efficiently separated at the interface between $CuFe_2O_4$ nanoparticles and MXene sheets due to their different band structures. This efficient charge separation reduces the recombination of electron-hole pairs and enhances the photocatalytic activity. So, it is expected degradation of methylene blue, methyl orange, and ibuprofen is enhanced in the present $CuFe_2O_4$@MXene nanoparticles.

On the other hand, the incorporation of graphitic carbon nitride (g-C_3N_4) into $CuFe_2O_4$@MXene further enhances the photocatalytic activity by extending the light absorption range and improving charge separation. g-C_3N_4 possesses a bandgap suitable for visible light absorption, complementing the light absorption range of $CuFe_2O_4$ and MXene. This extends the utilization of solar energy for photocatalytic reactions. In summary, MXene, $CuFe_2O_4$@MXene, and $CuFe_2O_4$@MXene/g-C_3N_4 exhibit enhanced photocatalytic activity for the degradation of methyl orange through a combination of light absorption, charge separation, and generation of reactive oxygen species, with each material contributing unique properties to the overall photocatalytic performance. This behavior was observed for methylene blue, methyl orange, and ibuprofen, respectively. In addition, the degradation kinetics curve was calculated for quasi-constant first-order kinetics, and the results are given in Table 2. Obtained values in Table 1 revealed that MXene shows better degradation for methylene blue compared to the other two compounds. $CuFe_2O_4$@MXene is less effective for methyl Orange but has a slightly better performance for Ibuprofen compared to MXene, while $CuFe_2O_4$@MXene/g-C_3N_4 shows the highest degradation rate for methylene blue, indicating it is the most effective for this compound among the materials tested. The rates for methyl orange and Ibuprofen are relatively comparable to other materials but still slightly higher. The results suggest that the $CuFe_2O_4$@MXene/g-C_3N_4 composite material generally performs better for methylene blue, while the other materials have varying effectiveness depending on the compound.

The possible degradation mechanism for methylene blue, methyl orange, and ibuprofen using the $CuFe_2O_4$@MXene/g-C_3N_4 composite material includes:

- **Light Absorption:** $CuFe_2O_4$ and g-C_3N_4 absorb light, exciting electrons to the conduction band.
- **Photoexcitation:** This excitation generates electron-hole pairs in both $CuFe_2O_4$ and g-C_3N_4.

Table 2. Degradation Rate Constants on the Prepared Samples

Samples	Methylene blue	Methyl orange	Ibuprofen
MXene	0.0069	0.0049	0.0029
$CuFe_2O_4$@MXene/	0.0065	0.0029	0.0043
$CuFe_2O_4$@MXene/g-C_3N_4	100.01188	0.0047	0.0048

- **Charge Transfer:** Electrons from the conduction bands of $CuFe_2O_4$ and g-C_3N_4 are transferred to MXene, which acts as an electron conductor.
- **Reactive Oxygen Species (ROS) Formation:** MXene facilitates the formation of ROS. Superoxide radicals ($O_2^{\bullet-}$) are formed from oxygen. Hydroxyl radicals (•OH) are formed from water.
- **Degradation of methylene blue (MB):** ROS, particularly hydroxyl radicals (•OH), attack methylene blue, breaking it down into intermediate products.
- **Mineralization:** The intermediate products are further decomposed into carbon dioxide (CO_2) and water (H_2O), completing the mineralization process.

CONCLUSION

In this study, a composite material consisting of $CuFe_2O_4$ doped MXene loaded on g-C_3N_4 was synthesized and thoroughly evaluated for its photocatalytic properties. The combination of these three components, MXene, $CuFe_2O_4$@MXene/g-C_3N_4, and $CuFe_2O_4$@MXene/g-C_3N_4, exhibited unique synergistic effects that significantly enhanced the photocatalytic degradation of various organic pollutants, including methylene blue, methyl orange, and ibuprofen. The incorporation of $CuFe_2O_4$ and g-C_3N_4 into the MXene matrix improved the photocatalytic performance. $CuFe_2O_4$ extended the light absorption range and facilitated efficient charge separation, while g-C_3N_4 complemented this effect by providing additional active sites and extending the light absorption range further into the visible spectrum. The $CuFe_2O_4$@MXene/g-C_3N_4 composite demonstrated superior photocatalytic efficiency compared to MXene alone or $CuFe_2O_4$@MXene. It exhibited the highest degradation rates for methylene blue, followed by relatively high performance for methyl orange and ibuprofen. This indicates that the composite is particularly effective for treating methylene blue but also performs well across other contaminants. The degradation kinetics followed quasi-first-order kinetics. The $CuFe_2O_4$@MXene/g-C_3N_4 composite showed the highest degradation rate for methylene blue, illustrating its superior catalytic efficiency compared to the other materials tested. For methyl orange and ibuprofen, the composite also displayed enhanced degradation rates, though the performance varied slightly depending on the compound.

ACKNOWLEDGEMENTS

The authors are grateful for the financial support from the Research Councils of Ilam University.

REFERENCES

[1] Kamgaing, T.; Doungmo, G.; Tchieno, F. M. M.; Kouonang, J. J. G.; Mbadcam, K. J., Kinetic and isotherm studies of bisphenol A adsorption onto orange albedo (*Citrus sinensis*): Sorption mechanisms based on the main albedo components vitamin C, flavones glycosides and carotenoids. *J. Environ. Sci. Health*, Part A **2017**, *52*, 757-769, DOI: org/10.1080/10934529.2017.1303315.

[2] Rashid, T., Sustainable wastewater treatment *via* dye-surfactant interaction: a critical review. *Ind. Eng. Chem. Res*. **2020**, *59*, 9719-9745, DOI: org/10.1021/acs.iecr.0c00676.

[3] Islam, M. A.; Islam, S. L.; Hassan, A., Impact of climate change on water with reference to the Ganges-Brahmaputra-Meghna River Basin. *J. Water Chem.* **2017**, 121-160, DOI: 10.1016/B978-0-12-809330-6.00003-9.

[4] Liu, W.; Moran, C. J.; Vink, S., A review of the effect of water quality on flotation, *Miner. Eng*. **2013**, *53*, 91-100, DOI: 10.1016/j.mineng.2013.07.011.

[5] Sharifi, F.; Ghasemian Lemraski, E.; Sharafinia, S., Super hydrophobic PU sponge modified by poly-vinylidene fluoride/SBA-15@NPS hybrid, *Soft Material*. **2023**, *22*, 41-53, DOI: org/10.1080/1539445X.2023.2288585.

[6] Ghasemian Lemraski, E.; Yari, S.; Khajeh Ali, E.; Sharafinia, S.; Jahangirian, H.; Rafiee-Moghaddam, R.; Webster. T. J., *J. Iran. Chem. Soc.* **2022**, *19*, 1287, DOI.org/10.1007/s13738-021-02382-x.

[7] Sharafinia, S.; Farrokhnia, A.; Ghasemian Lemraski, E., The adsorption of cationic dye onto ACPMG@ZIF-8 core-shell, optimization using central composite response surface methodology (CCRSM). *Colloids Surf. A: Physicochem. Eng. Asp*. **2022**, *634*, 128039, DOI: org/10.1016/j.colsurfa.2021.128039.

[8] Chegeni, M.; Nasrollahi, F., Construction of ZnS/montmorillonite/graphitic Carbon Nitride as Adsorbent and Photocatalyst for the Removal of Rhodamine B. *Phys. Chem. Res.* **2024**, *12*(2), 273-287, DOI: 10.22036/pcr.2023.377475.2258.

[9] Dwijenra, N. K. A.; Patra, I.; Ansari, M. J.; Saadoon, N.; Al Mashhadani, Z. I.; Obaid, N. H.; Sivaraman, R.; Alawsi, T.; Jabbar, A. H.; Mustafa, Y. F., Insights into the Electronic Properties of Coumarins: A Comparative Study Synthesis and Characterization of Fe_2O_3/Mn_2O_3 Magnetic Nanocomposites for the Photocatalytic Degradation of Methylene Blue. *Phys. Chem. Res.* **2023**, *11*(2), 437-447. DOI: 10.22036/pcr.2022.336018.2070.

[10] Yan, S.; Li, Z.; Zou, Z. G., Photodegradation of rhodamine B and methyl orange over boron-doped g-C_3N_4 under visible light irradiation. *Langmuir*, **2010**, *26*, 3894–3901, DOI.org/10.1021/la904023j.

[11] Rakibuddin, M.; Kim, H.; Khan, M. E., Graphite-like carbon nitride (C_3N_4) modifed N-doped $LaTiO_3$ nanocomposite for higher visible light photocatalytic and photo-electrochemical performance. *Appl. Surf. Sci.* **2018**, *452*, 400-412, DOI: org/10.1016/j.apsusc.2018.05.018.

[12] Wu, Y.; Wang, H.; Tu, W.; Liu, Y.; Zen Tan, Y.; Yuan, X.; Wei Chew, J., Quasi-polymeric construction of stable perovskite-type $LaFeO_3$/g-C_3N_4 heterostructured photocatalyst for improved Z-scheme photocatalytic activity via solid pn heterojunction interfacial effect. *J. Hazard. Mater*. **2018**, *347*, 412-422, DOI: org/10.1016/j.jhazmat.2018.01.025.

[13] Tahmasebi, Z.; Ghasemian Lemraski, E., Ternary zinc oxide-tungsten oxide-MXenes nanocomposite as a high performance material for photocatalytic and photo-electrocatalytic desulfurization of dibenzothiophene. *Electrochem. commun.* **2025**, *177*, 107933, DOI: org/10.1016/j.elecom.2025.107933.

[14] Zhang, L.; Sua, W.; Shu, H.; Lüa, L.; Fua, T.; Songc, K.; Huangc, X.; Yud, J.; Lind, C. -Te.; Tang, Y., Tuning the photoluminescence of large Ti_3C_2Tx MXene flakes. *Ceram. Int*. **2019**, *45*, 11468-11474, DOI: org/10.1016/j.ceramint.2019.03.014.

[15] Lan, K.; Liu, Y.; Zhang, W.; Liu, Y.; Elzatahry, A.; Wang, R.; Xia, Y.; Al-Dhayan, D.; Zheng, N.; Zhao, D., Uniform ordered two-dimensional mesoporous TiO_2 nanosheets from hydrothermal-induced solvent-confined monomicelle assembly. *J. Am. Chem. Soc*. **2018**, *140*, 4135-4143, DOI: org/10.1021/jacs.8b00909.

[16] Naguib, M.; Kurtoglu, M.; Presser, V.; Lu, J.; Niu, J.; Heon, M.; Hultman, L.; Gogotsi, Y.; Barsoum, M. W., Two-Dimensional Nanocrystals Produced by Exfoliation of Ti_3AlC_2. *Adv. Mater*. **2011**, *23*, 4248-4253. DOI: 10.1002/adma.201102306.

[17] He, F.; Zhu, B.; Cheng, B.; Yu, J.; Ho, W.; Macyk, W., 2D/2D/0D $TiO_2/C_3N_4/Ti_3C_2$ MXene composite S-scheme photocatalyst with enhanced CO_2 reduction activity. *Appl. Catal. B: Environ*. **2020**, *272*, 119006, DOI: org/10.1016/j.apcatb.2020.119006.

[18] Li, J.; Wang, Y.; Wang, Y.; Guo, Y.; Zhang, S.; Song, H.; Li, X.; Gao, Q.; Shang, W.; Hu, S.; Zheng, H.; Li, X., MXene Ti_3C_2 decorated g-C_3N_4/ZnO photocatalysts with improved photocatalytic performance for CO_2 reduction. *Nano Mater. Sci.* **2023**, *5*, 237-245, DOI: org/10.1016/j.nanoms.2023.02.003.

[19] Mishra, R. P.; Mrinalini, M.; Kumar, N.; Bastia, S.; Chaudhary, Y. S., Efficient Photocatalytic CO_2 Reduction with High Selectivity for Ethanol by Synergistically Coupled MXene-Ceria and the Charge Carrier Dynamics. *Langmuir*, **2023**, *39*, 14189-14203. DOI: org/10.1021/acs.langmuir.3c01064.

[20] Xiao, W.; Xu, W.; Huang, W.; Zhou, Y.; Jin, Z.; Wei, X.; Li, J., Bismuth-Based BiOBrxI1–x/Ti_3C_2 MXene Schottky Nanocomposites for Hg^{2+} Photoelectrochemical Sensors. *ACS Appl. Nano*

Mater. **2022**, *5*, 18168-18177, DOI: org/10.1021/acsanm.2c04063.

[21] Zhao, S.; Pan, D.; Liang, Q.; Zhou, M.; Yao, C.; Xu, S.; Li. Z., NiAl-Layered Double Hydroxides Grown on 2D Ti_3C_2Tx MXene to Construct Core-Shell Heterostructures for Enhanced Photocatalytic CO_2 Reduction. *J. Phys. Chem. C*. **2021**, *125*, 10207-10218, DOI: org/10.1021/acs.jpcc.1c00017.

[22] Halim, J.; Cook, K.M.; Naguib, M.; Eklund, P.; Gogotsi, Y.; Rosen, J.; Barsoum, M. W., X-ray photoelectron spectroscopy of select multi-layered transition metal carbides (MXenes). *Appl. Surf. Sci*. **2016**, *362*, 406-417, DOI: org/10.1016/j.apsusc.2015.11.089.

[23] Harris, K. J.; Bugnet, M.; Naguib, M.; Barsoum, M. W.; Goward, G. R., Direct measurement of surface termination groups and their connectivity in the 2D MXene V_2CTx using NMR spectroscopy. *J. Phys. Chem. C* **2015**, *119*, 13713-13720, DOI: org/10.1021/acs.jpcc.5b03038.

[24] Kang, R.; Zhang, Z.; Guo, L.; Cui, J.; Chen, Y.; Hou, X.; Wang, B.; Lin, C. -T.; Jiang, N.; Yu, J., Enhanced Thermal Conductivity of Epoxy Composites Filled with 2D Transition Metal Carbides (MXenes) with Ultralow Loading. *Sci. Rep*. **2019**, *9*, 9135, DOI: 10.1038/s41598-019-45664-4.

[25] Xue, Q.; Zhang, H.; Zhu, M.; Pei, Z.; Li, H.; Wang, Z.; Huang, Y.; Huang, Y.; Deng, Q.; Zhou, J.; Du, S.; Huang, Q.; Zhi, C., Photoluminescent Ti_3C_2 MXene Quantum Dots for Multicolor Cellular Imaging. *Adv., Mater*. **2017**, *29*, 1604847, DOI: 10.1002/adma.201604847.

[26] Li, Y.; Zhou, X.; Wang, J.; Deng, Q.; Li, M.; Du, S.; Han, Y. -H.; Lee, J.; Huang, Q., Facile preparation of in situ coated $Ti_3C_2TX/Ni0.5Zn0.5Fe_2O_4$ composites and their electromagnetic performance. *RSC Adv*. **2017**, *7*, 24698-24708, DOI: org/10.1039/C7RA03402D.

[27] Iqbal, A.; Shahzad, F.; Hantanasirisakul, K.; Kim M. K.; Kwon, J.; Hong, J.; Kim, H.; Kim, D.; Gogotsi, Y.; Koo, C. M., Anomalous absorption of electromagnetic waves by 2D transition metal carbonitride $Ti_3CNTxMXene$. *Science*. **2020**, *24*, 446-450, DOI: 10.1126/science.aba7977.

[28] Sarycheva, S.; Gogotsi, Y., Raman spectroscopy analysis of structure and surface chemistry of Ti_3C_2Tx MXene. *Chem. Mat.* **2020**, *32*, 3480-3488, DOI. 10.1021/acs.chemmater.0c00359.

[29] Sabari Girisun, T. C.; Saravanan, M.; Venugopal Rao, S., Femtosecond nonlinear absorption and optical limiting action in nanoplatelet $CuFe_2O_4$-decorated rGO nanocomposites. *Appl. Sci.* **2019**, *1*, 400, DOI: org/10.1007/s42452-019-0408-5.

[30] Shuck, C. E.; Ghidiu, M. J.; Frey, N. C.; Anasori, B., Direct Observation of Cation Intercalation in MXenes Using Raman Spectroscopy. *ACS Nano*, **2021**, *15*, 1543-1551, DOI: org/10.1016/j.cej.2023.145526.

[31] Yedah Afsheen, Z.; Murshed, M. M/; Naeem, U.; Gesing, T. M.; Rizwan, S., Cation-assisted self-assembled pillared V2CTx MXene electrodes for efficient energy storage. *Chem. Eng. J*. **2023**, *474*, 385-8947, DOI: org/10.1016/j.cej.2023.145526.

[32] Ghidiu, M.; Lukatskaya, M. R.; Zhao, M. Q.; Gogotsi, Y.; Barsoum, M. W., Conductive two-dimensional titanium carbide 'clay' with high volumetric capacitance. *Nature*. **2014**, *516*, 78-81, DOI: org/10.1038/nature13970.

[33] Zhang, F.; Li, X.; Zhao, Q.; Chen, A., Facile and Controllable Modification of 3D In_2O_3 Microflowers with In_2S_3 Nanoflakes for Efficient Photocatalytic Degradation of Gaseous ortho-Dichlorobenzene. *J. Phys. Chem.* C **2016**, *120*, 19113-19123. DOI: org/10.1021/acs.jpcc.6b03618.

[34] Caoa, Y.; Fanga, Y.; Leia, X.; Tana, B.; Huc, X.; Liuc, B.; Chena, Q., Fabrication of novel $CuFe_2O_4$/MXene hierarchical heterostructures for enhanced photocatalytic degradation of sulfonamides under visible light. *J. Hazard. Mater*. **2020**, *387*, 122021. DOI: org/10.1016/j.jhazmat.2020.122021.

[35] Pournemati, K.; Habibi-Yangjeh, Az., Recent insights on Z-scheme and S-scheme photocatalysts for nitrogen conversion to ammonia: A review. Mater. Today Sustain**.** **2024**, *28*, 101043, DOI.: org/10.1016/j.mtsust.2024.101043.

[36] Seifikar, F.; Habibi-Yangjeh, A.; Jahed-Jaafargolikhanlo, M., A critical review on emerging photothermal-photocatalytic materials composed of g-C_3N_4 for energy production and environmental

remediation. *J. Environ. Chem. Eng.*, **2025**, *13*, 2213-3437, DOI: org/10.1016/j.jece.2025.115812.

[37] Habibi-Yangjeh, A.; Pournemati, K., A review on emerging homojunction photocatalysts with impressive performances for wastewater detoxification. *Crit. Rev. Environ. Sci. Technol.* 2024, *54*, 290-320, DOI: org/10.1080/10643389.2023.2239125.

[38] Seifikar, F.; Habibi-Yangjeh, A., Floating photocatalysts as promising materials for environmental detoxification and energy production: A review, *Chemosphere*. **2024**, *355*, 141686, DOI: org/10.1016/ j.chemosphere.2024.141686.

[39] Vassiliou, J. K.; Mehrotra, V.; Russell, M. W.; Giannelis, E. P.; McMichael, R. D.; Shull, R. D.; Ziolo, R. F., Magnetic and optical properties of γ-Fe_2O_3 nanocrystals, *J. Appl. Phys*. **1993**, *73*, 5109, DOI: org/10.1063/1.353784.

[40] Eskandarloo, H.; Badiei, A., Photocatalytic application of Titania nanoparticles for degradation of organic pollutants. *Nanotechnol Opt. Sens*. **2021**, *130*, 108-111, DOI: org/10.1016/j.inoche.2021.108688.